Supporting Information for

Enhancing perovskite detector performance via bias-induced aging: a reproducible and universal approach

Qingli Zhang,†[a] Jincong Pang,†*[a] Shunsheng Yuan,†[a] Zhiqiang Liu,[a] Lin Li,[b] Kai Gao,[b] Fangke Chen,[a] Zhongyu Yang,[a] Ying Zhou,[a] Guangda Niu,[a] Ling Xu,*[a] Jiang Tang[a]

[a] Wuhan National Laboratory for Optoelectronics and School of Optical and Electronic Information, Huazhong University of Science and Technology, Wuhan 430074, China.

[b] Institute of New Materials and Advanced Manufacturing, Beijing Academy of Science and Technology, Beijing 100089, China.

E-mail: jpang@hust.edu.cn, xuling@mail.hust.edu.cn

† These authors contributed equally, Qingli Zhang, Jincong Pang, Shunsheng Yuan

Methods

Materials

Cesium bromide (CsBr, 99.999%), Formamidinium bromide (FABr, 99.999%), methylammonium bromide (MABr, 99.999%), and lead bromide ($PbBr_2$, 99.999%) were purchased from Liaoning Youxuan Co., Ltd. N,N-dimethylformamide (DMF) and dimethyl sulfoxide (DMSO) were purchased from Sigma-Aldrich. All chemicals were of analytical grade and used as received without further purification. Gold (Au, 99.999%), titanium (Ti, 99.999%), lead (Pb, 99.999%), and bismuth (Bi, 99.999%) particles were supplied by ZhongNuo Advanced Materials (Beijing) Co., Ltd.

Synthesis and Crystal Growth

A. Growth of $CsPbBr_3$ Single Crystals via the Bridgman Method

High-purity CsBr and $PbBr_2$ powders were mixed in a 1:1 molar ratio and loaded into a quartz ampoule with an outer diameter of 15 mm and an inner diameter of 12 mm. The ampoule was evacuated to a pressure of 1×10^{-4} Pa and sealed using an oxyhydrogen flame. The sealed ampoule was placed in a muffle furnace, heated to 650 °C at a rate of 2 °C min^{-1}, and maintained at this temperature for 12 h to ensure complete melting, reaction, and homogenization of the raw materials. Subsequently, the melt was cooled at a rate of 5–15 °C min^{-1} to initiate crystallization.

The pre-treated ampoule was then transferred to a custom-built six-zone vertical Bridgman furnace. The system was heated for 10 h to reach the target temperature, establishing a temperature gradient of approximately 15 K cm^{-1}. During the initial stage, the ampoule was overheated to 600 °C and held for 12 h to further homogenize the melt. Crystal growth was then carried out by lowering the ampoule along the furnace axis at a slow rate of 0.3 mm h^{-1}.

The obtained $CsPbBr_3$ ingots were cut into wafers with dimensions of 8 × 8 × 2 mm^3 and 20 × 8 × 2 mm^3 using a diamond wire saw (STX-202A, Hefei Kejing Materials Technology Co., Ltd.). The crystal surfaces were sequentially polished using nonwoven abrasive papers with grit sizes of 1000, 2000, 5000, and 12000 to achieve a smooth and mirror-like finish.

B. Growth of $APbBr_3$ (A = Cs, FA, MA, $Cs_{0.1}FA_{0.9}$) Single Crystals via Solution

Method

Stoichiometric amounts of ABr (A = Cs, FA, MA, $Cs_{0.1}FA_{0.9}$) and $PbBr_2$ were dissolved in a mixed solvent of GBL, DMF and DMSO at 60–70 °C to form a saturated and clear precursor solution. The solution was filtered through a 0.22 μm PTFE membrane and transferred into a clean glass dish. Single crystals were grown by slow cooling at a rate of 2 °C h^{-1} down to room temperature under a nitrogen atmosphere. The as-grown crystals were washed three times with anhydrous ethanol and dried in a vacuum oven at 60 °C for 12 h. The resulting single crystals typically reached sizes exceeding $10 \times 10 \times 5$ mm^3. Prior to device fabrication, the crystal surfaces were successively polished with abrasive papers from 1000 to 12000 grit to obtain a mirror-smooth surface. For full experimental details of the mixed-A-site compositional series and growth conditions, readers can find more information in our recently published paper (DOI: 10.1038/s41566-026-01849-8), where the synthesis protocol and compositional series are reported (such as $Cs_{0.15}FA_{0.85}$, $Cs_{0.25}FA_{0.75}$, $Cs_{0.5}FA_{0.5}$).

Detector Electrode Configuration

Three types of metal–semiconductor–metal (MSM) radiation detectors were fabricated, including asymmetric Schottky-contact devices with Bi/$APbBr_3$/Au, Bi/$APbBr_3$/C, Pb/$APbBr_3$/Au, and Ti/$APbBr_3$/Au configurations, a double-Schottky-contact Bi/$APbBr_3$/Bi structure, as well as double-Ohmic-contact devices with an Au/$APbBr_3$/Au structure. The Au, Pb, and Bi electrodes were deposited by thermal evaporation with a thickness of 70-100 nm, while the Ti electrodes were fabricated by electron-beam evaporation with a thickness of 50-70 nm. For the carbon electrode, a thin layer of conductive carbon paste was directly applied onto the crystal surface and dried under ambient conditions. It is worth noting that only the Schottky-type devices were subjected to long-term bias aging in the experiment in Figure 3. To investigate the intrinsic evolution of the perovskite crystal under a sustained electric field, the original electrodes were removed after the aging process, and new Au/$APbBr_3$/Au electrodes were redeposited for subsequent measurements. This approach effectively eliminates the influence of interfacial instability on the device performance evaluation.

We also conducted aging tests on the devices with double-Schottkys and double-ohms in Figure S2.

Test Environment

Unless otherwise stated, all electrical (*I–V* and *I–t*), X-ray photoresponse, and γ-ray energy-spectrum measurements were carried out in Wuhan, China, at room temperature under ambient laboratory atmosphere. During the measurement period, the relative humidity typically fluctuated in the range of 60–80%, and all datasets reported in this work were acquired under these conditions. Notably, we and our collaborators independently observed the same reverse-bias-aging behavior and performance enhancement trends in different cities, including Jinan, Beijing, and Shenzhen (China), suggesting that the phenomenon is robust across typical indoor ambient environments.

X-ray Detection Test

The electrical and photoresponse characteristics of the devices were measured using a Keithley 6517B electrometer under various bias polarities and magnitudes. For X-ray detection, the devices were irradiated with photons generated from an Amptek Mini-X2 X-ray tube (gold target, Model M237, Newton Scientific Co.). The photocurrent and dark current were recorded to evaluate the photo-to-dark current ratio, which reflects the detector’s sensitivity to X-ray irradiation.

Energy Spectrum Measurement

The γ-ray spectra were acquired using an AMETEK ORTEC NIM-based pulse-signal acquisition and analysis system (NIM power supplies and bins). A high-voltage power supply (ORTEC 556), a spectroscopy amplifier (ORTEC 672), and a multichannel analyzer (ORTEC 928) were used, and the spectra were collected and exported using the MAESTRO software. Unless otherwise stated, all spectra reported in this work were measured under identical conditions with a shaping time of 3 μs, an amplifier gain of 500, and an applied electric field of 400 V mm^{-1}.

To evaluate the energy resolution, detectors subjected to different biasing durations and polarities were exposed to a standard radioactive source (^{137}Cs). The resulting spectra were fitted using a Gaussian function to extract the full width at half maximum (FWHM, ΔE). The energy resolution (ER) was calculated using the equation:

$$ER = \frac{\Delta E}{E} \times 100\%$$

where E is the centroid energy of the photopeak. A smaller ER value indicates superior energy discrimination capability of the detector.

Time-of-Flight (ToF) Measurement of Carrier Mobility

Carrier mobility was measured using the time-of-flight (ToF) technique under pulsed laser excitation. A 337 nm pulsed nitrogen laser was used as the excitation source. Bias voltages of 8, 20, and 50 V were applied across the device to induce carrier drift within the crystal.

The carrier transit time was determined from the inflection point of the transient current curve, and the mobility (μ) was calculated according to the formula:

$$\mu = \frac{d^2}{\tau V}$$

where d is the electrode spacing, V is the applied voltage, and τ is the transit time. Measurements were performed on the device in three different states: as-fabricated, after reverse bias aging, and after forward bias aging. The results were used to compare the effects of bias-induced aging on the charge transport characteristics of $CsPbBr_3$ single crystal detectors.

Thermally Stimulated Current (TSC) Measurement

Thermally stimulated current (TSC) measurements were conducted to analyze the trap states in $CsPbBr_3$ single-crystal devices. The Au/$CsPbBr_3$/Bi planar detectors were first cooled to 88 K using liquid nitrogen and maintained at this temperature to freeze the charge carriers. After thermal stabilization, the devices were illuminated by an X-ray source for 5 minutes to ensure that the defect states were sufficiently filled with photogenerated electrons and holes.

Subsequently, the X-ray source was turned off, and the devices were heated from 88 K to 273 K at a constant rate of 0.1 K s^{-1}. During the heating process, the trapped carriers were thermally released and drifted under the internal field, generating a transient current signal. The thermally stimulated current spectra were recorded using a Keithley 6517B electrometer connected to the device. The obtained TSC curves reflect the distribution and density of trap states before and after bias-induced aging.

Kelvin Probe and SCLC Characterization

Surface potential measurements were performed using a Kelvin probe force microscope (KPFM, Ntegra Prima KFM) to monitor the evolution of the crystal surface potential before and after bias aging. To further investigate charge transport dynamics, the space-charge-limited current (SCLC) characteristics of the Au/$CsPbBr_3$/Au devices were measured before and after the bias treatment.

When the applied voltage exceeds the trap-filled limit, the injected carrier density surpasses the intrinsic carrier concentration, leading to the formation of a space-charge region that restricts further current increase. In this regime, the current density exhibits a quadratic dependence on the electric field, following the relationship:

$$J = \frac{9}{8} \times \frac{\varepsilon \mu E^2}{d}$$

where J is the current density, ε is the dielectric constant of the material, μ is the carrier mobility, E is the electric field strength, and d is the electrode spacing. By fitting the dark current–voltage (I–V) curves in double-logarithmic coordinates, the slope transitions were analyzed to identify the SCLC-dominated region, enabling quantitative extraction of the carrier mobility and trap density.

Stability test

We have added stability evaluations of bias-aged devices under (i) continuous irradiation (operational stability) and (ii) room-temperature storage, and we monitored the evolution of dark current, energy resolution (ER), and the photo-to-dark current ratio. (i) Operational stability under continuous irradiation. Bias-aged devices were continuously irradiated with a ^{137}Cs source for 10 days while maintaining the reverse-bias aging condition. Throughout the entire irradiation period, the devices exhibit no obvious degradation in spectral response or ER. These results demonstrate excellent operational stability of the bias-aged detectors under sustained radiation exposure.

The corresponding data and plots have been added as Figure S6 in the revised Supporting Information. (ii) Stability during room-temperature storage. We further evaluated retention of the bias-aging-induced performance gain after removing the bias. Specifically, after the aging treatment, the bias was removed and the devices were stored at room temperature for 10 days, during which key metrics were measured at multiple time points. We observed a moderate performance relaxation during storage; however, even after 10 days, the dark current, photo-to-dark current ratio, and ER remain substantially improved compared with the pre-aged state, indicating that the performance enhancement is reasonably retained. These results have been included as Figure S7.

DFT Calculations of Defect Formation Energies

Density functional theory (DFT) calculations were performed to investigate the electronic structures and defect formation energies of $APbBr_3$ (A = Cs, FA, MA) perovskites. The plane-wave basis set was employed to expand the electronic wavefunctions [1], and the exchange–correlation energy was described within the framework of the generalized gradient approximation (GGA) [2-4] using the Perdew-Burke-Ernzerhof (PBE) functional [5,6].

All self-consistent electronic calculations were converged to an energy threshold of 10^{-6} eV, while atomic positions and lattice parameters were optimized until the residual forces were smaller than 0.02 eV $Å^{-1}$. The Brillouin zone was sampled using the Γ-centered Monkhorst–Pack k-point mesh, with a k-point spacing of $0.02 \times 2\pi$ $Å^{-1}$, and a kinetic energy cutoff of 450 eV was applied for the plane-wave expansion. Convergence tests with respect to both k-point density and energy cutoff were carefully conducted to ensure numerical accuracy.

The formation energy of a defect D in charge state q was calculated using the expression:

$$E^f[D] = E_{tot}[D,q] - E_{tot}[bulk] \pm n\mu_i + q[\varepsilon_F + \varepsilon_{VBM} + \Delta V]$$

where $E_{tot}[bulk]$ and $E_{tot}[\mathrm{D},q]$ are the total energies of the perfect supercell and of the defective supercell containing the defect in the charge state q. μ_i is the chemical potential of atom species i (such as Cs, Pb, or Br), n is the number of atoms added or removed, if adding an atom, take a negative sign, and if not, take a positive sign. ε_F is the Fermi level reference to the valence-band maximum (VBM), ε_{VBM}. An alignment procedure (ΔV) is adopted to align the averaged electrostatic potentials between the defective supercell and the host.

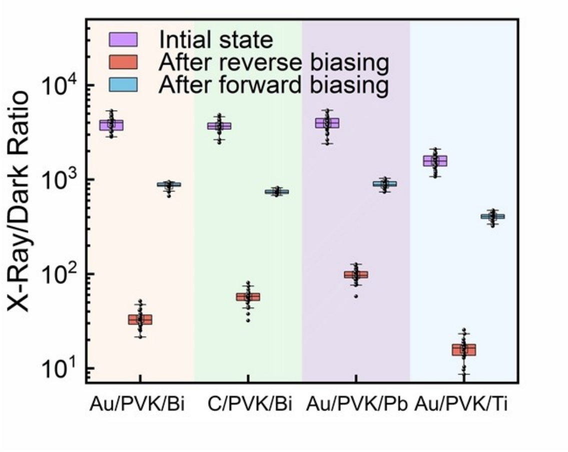

Figure S1. Changes in rectification ratio of devices with different electrode materials in the initial state, after long-term reverse bias, and after long-term forward bias. Rectification ratio of MSM devices with different electrodes in the pristine state and after reverse/forward bias aging (±200 V, 12 h).

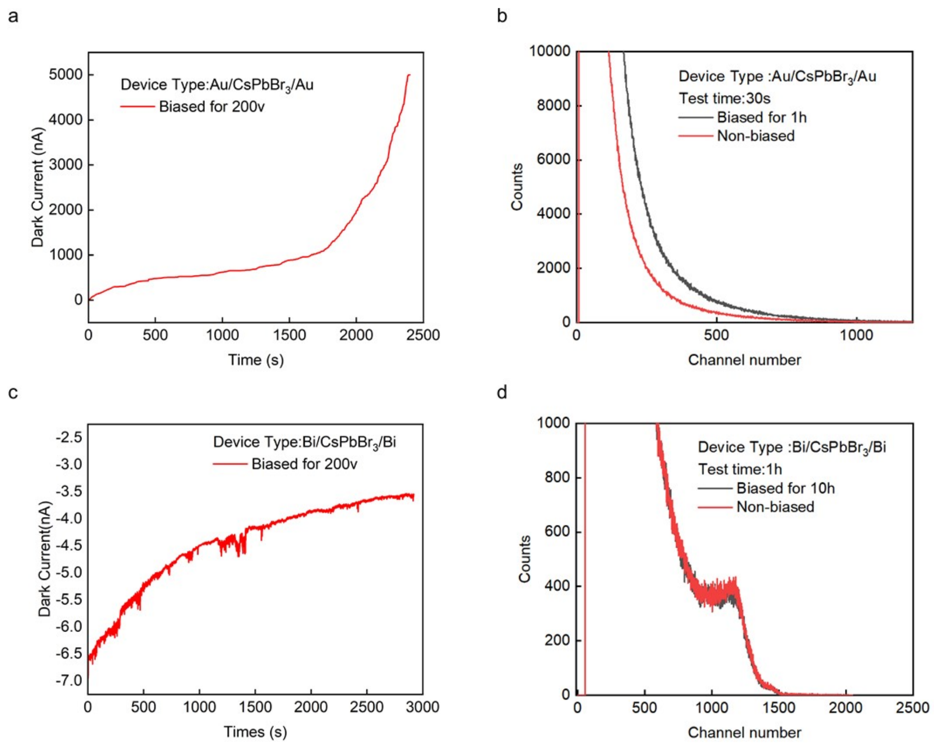

Figure S2. Bias-aging behavior of ohmic- and Schottky-contact devices. (a) Dark-current evolution of the double-ohmic Au/FAPbBr$_3$/Au device during bias aging. (b) ^{137}Cs spectrum measured after bias aging of the double-ohmic device (noise-dominated, preventing reliable spectrum acquisition). (c) Dark-current evolution of the double-Schottky Bi/FAPbBr$_3$/Bi device during bias aging. (d) ^{137}Cs spectrum measured after bias aging of the double-Schottky device. The proposed bias-aging strategy is most effective and experimentally viable for asymmetric Schottky-type devices with suppressed injection current. In contrast, double-ohmic devices can suffer rapid leakage/noise escalation, and double-Schottky devices show dark-current suppression but limited improvement in charge-collection and spectral metrics under our conditions (Figure S2).

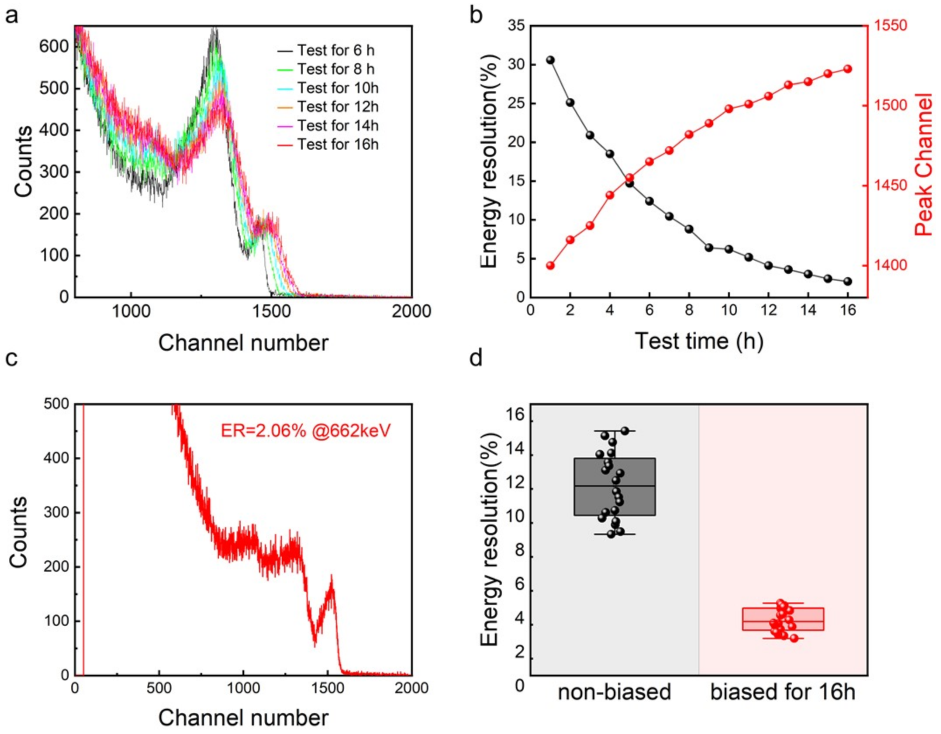

Figure S3. The gamma-ray spectra characteristics of $FAPbBr_3$ devices after bias-induced aging. (a) The change of ^{137}Cs energy spectra after reverse bias, with 3 μs shaping time. (b) The change of energy resolution and full-energy photopeak peak channel after reverse bias. (c) Test results of the highest energy resolution. (d) Statistical results of the energy resolution variation of the Au/$FAPbBr_3$/Bi device after 16 hours of reverse bias aging.

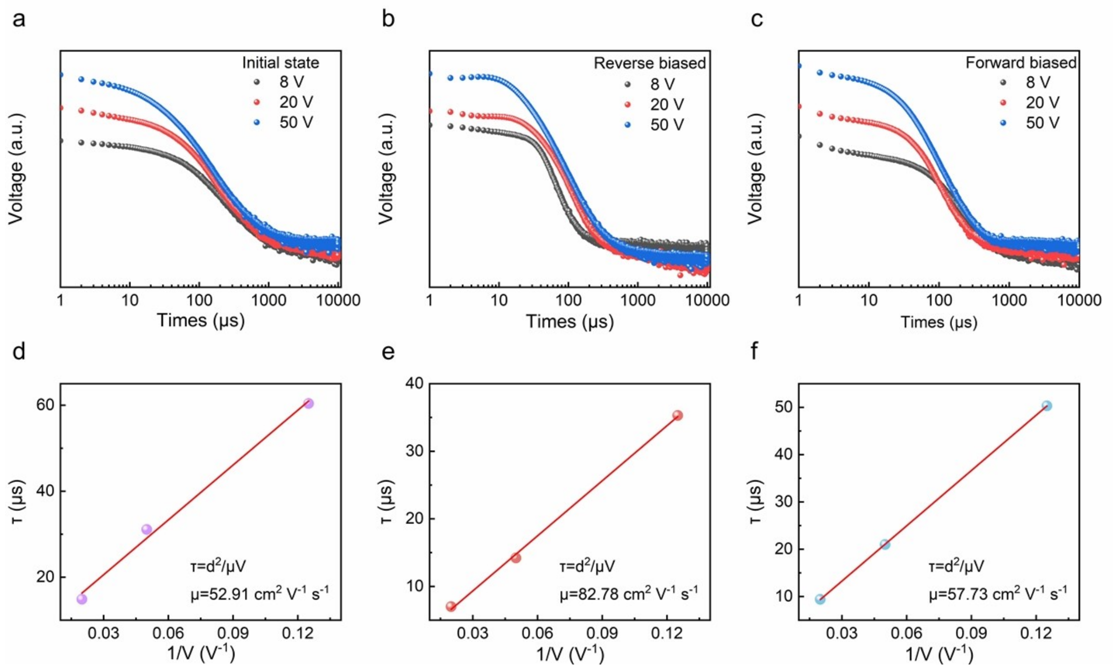

Figure S4. Time-of-flight charge transient curves of the device in (a) the initial state, (b) after reverse bias aging, and (c) after forward bias aging. (d), (e), and (f) show the corresponding charge transfer time versus reciprocal bias voltage.

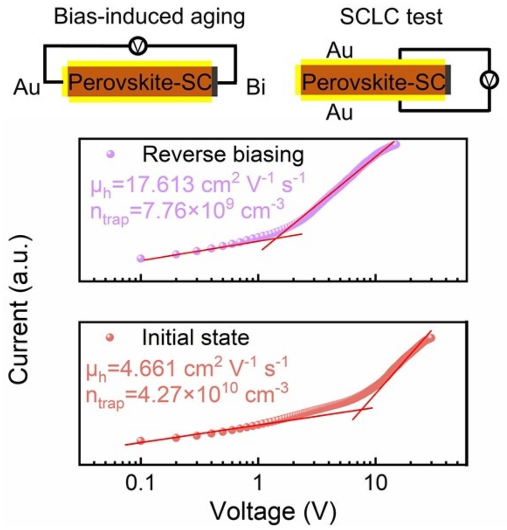

Figure S5. Changes in defect density before and after bias aging (SCLC characteristics).

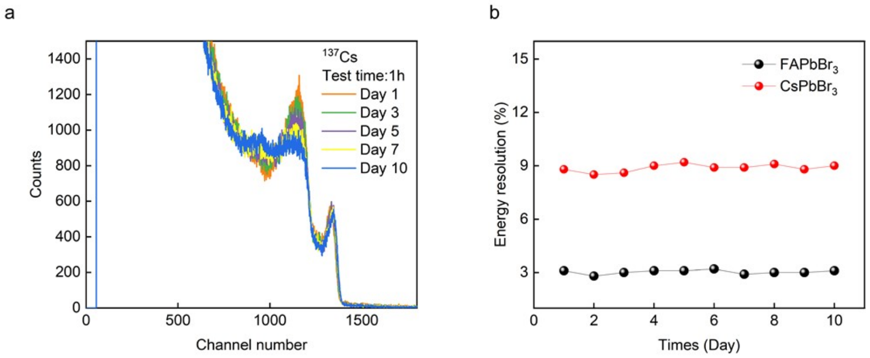

Figure S6. Operational stability of bias-aged devices under continuous ^{137}Cs irradiation. (a) Evolution of the ^{137}Cs spectra during continuous irradiation under −200 V. (b) Evolution of energy resolution (ER) during continuous irradiation.

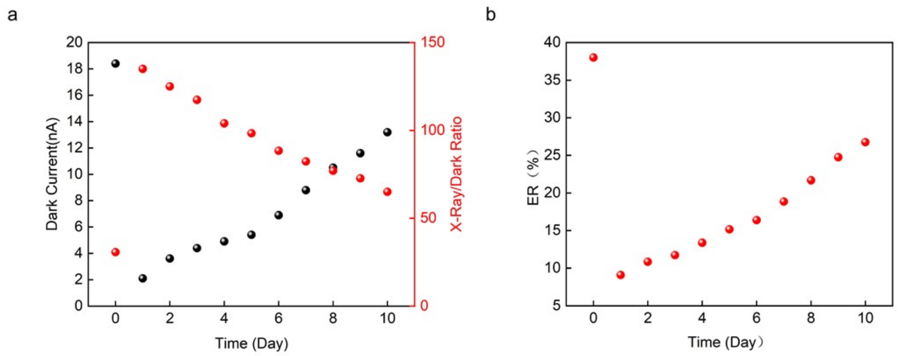

Figure S7. Stability of bias-aged devices during room-temperature storage after bias removal. (a) Evolution of dark current and photo-to-dark current ratio over storage time. (b) Evolution of ER over storage time.

Table S1. Parameter information regarding bias-induced aging

experimental situation	bias voltage (V)	bias voltage time	bias voltage interval
Figure 1a	+200 V (forward) −200 V (reverse)	4 h	0
Figure 1b	+200 V (forward) −200 V (reverse)	3.5 h	0
Figure 1c	-200	5 min for each cycle	5 min
Figure 1d	-200	20 min	0
Figure 1e/f	-200	12 h	0
Figure 2a/b/c	-200	60 min	0
Figure 2d	200	60 min	0
Figure 3a	200/-200	4 h	0
Figure 3b/c/d	-200	12 h	0
Figure S1	-200	12 h	0
Figure S2	-200	16 h	0
Figure S3	-200	12 h	0
Figure S4	-200	8 h	0

Table S2. Test results after 12 hours of aging. All measurements were performed under the same X-ray tube settings. The samples in Group A/B refer to single-crystal devices obtained from two other research groups. The sign of improvement was consistent across all measured working devices.

Sample name	Sample source	Dark current before aging/nA	Dark current after aging/nA	X-ray light-dark ratio before aging	X-ray light-dark ratio after aging
m-$CsPbBr_3$	Our group	5.13	0.53	24.73	134.62
		15.87	1.87	58.12	251.09
		9.42	1.14	31.06	178.45
		12.06	0.76	47.89	213.77
		7.59	1.65	20.45	146.03
		10.33	0.92	39.27	199.58
		14.71	1.28	55.64	242.16
		6.28	1.99	26.98	160.94
		11.94	0.61	42.11	225.31
		8.07	1.43	33.5	187.66
		13.65	0.58	59.83	255.72
		5.98	1.72	28.04	139.28
		15.12	0.85	46.37	208.9
		9.86	1.09	21.92	152.41
		7.14	1.56	52.76	236.85
		10.79	0.97	37.18	171.07
		12.53	1.33	44.59	219.53
		6.77	0.69	29.71	164.89
		14.09	1.91	59.97	248.34
		11.21	1.21	23.38	141.15
		8.95	0.74	41.85	202.76
		13.08	1.48	35.09	193.02
		5.47	0.52	57.46	230.68
		15.64	1.83	30.62	156.97
		9.03	1.16	49.14	214.26
		7.88	0.89	22.07	132.58
		10.11	1.62	54.31	240.91
		12.97	0.66	38.66	181.39
		6.05	1.05	45.22	223.04
		14.83	1.94	27.53	167.73
		11.58	0.79	51.08	246.55
		8.22	1.09	34.97	149.86
		13.91	0.57	56.79	206.13
		5.76	0.77	25.16	158.6
		15.03	1.12	48.03	237.49
		9.67	0.95	32.74	175.22
		7.31	1.58	53.9	228.97
		10.56	0.63	36.41	136.4
		12.19	1.26	40.58	211.88
		6.93	0.88	43.07	190.57
Sample name	Sample	Dark	Dark	X-ray light-	X-ray light-dark

	source	current before aging/nA	current after aging/nA	dark ratio before aging	ratio after aging
w-$CsPbBr_3$	Our group	13.47	4.73	11.49	67.42
		21.08	7.18	9.03	28.71
		16.92	6.05	25.72	44.56
		12.36	4.29	11.49	19.44
		19.75	7.62	25.19	66.68
		14.11	5.11	12.38	39.79
		20.63	6.84	9.64	44.84
		17.29	4.57	6.74	58.25
		15.58	7.39	13.72	58.58
		21.94	5.96	34.66	40.61
		18.04	6.21	22.87	72.58
		12.87	4.88	16.45	46.27
		19.12	7.04	35.76	95.61
		16.03	5.63	29.51	37.84
		13.91	6.77	12.34	73.92
		20.27	4.12	38.67	59.14
		14.66	7.55	28.92	88.45
		17.88	5.28	15.58	61.73
		21.37	6.49	34.21	34.36
		15.09	4.94	30.47	94.99
	Group A	17.42	13.58	8.47	40.73
		58.79	8.21	19.84	59.18
		33.06	11.47	12.11	52.46
		46.15	9.06	16.99	47.09
		20.93	12.93	9.66	58.62
		54.37	10.34	18.32	44.31
		28.64	8.79	10.45	55.08
		39.81	13.12	14.78	41.97
		59.08	9.65	11.93	49.85
		25.27	11.08	17.22	57.24
	Group B	12.47	11.34	5.73	20.56
		68.23	39.18	14.18	20.73
		95.86	21.07	12.46	29.18
		119.04	33.62	7.09	22.46
		73.51	24.95	13.62	27.09
		104.39	38.41	6.31	22.62
		61.78	29.76	10.08	24.31
		88.12	20.83	8.97	25.08
		116.65	35.09	11.85	21.97
		79.97	26.58	9.24	23.85
Sample name	Sample source	Dark current before aging/nA	Dark current after aging/nA	X-ray light-dark ratio before aging	X-ray light-dark ratio after aging
$FAPbBr_3$	Our group	2.13	0.23	88.23	341.36

		4.87	0.78	78.26	335.68
		3.46	0.41	73.50	343.55
		2.79	0.67	71.37	312.63
		4.12	0.35	66.83	340.67
		2.58	0.56	93.67	414.86
		3.91	0.29	77.35	315.27
		4.35	0.73	71.55	394.96
		2.24	0.62	79.79	405.69
		4.68	0.48	77.75	335.36
		3.07	0.25	79.81	329.44
		2.95	0.79	78.34	361.44
		4.53	0.33	67.19	316.02
		3.62	0.58	106.27	311.59
		2.41	0.44	72.56	312.01
		4.09	0.71	70.73	367.56
		3.28	0.27	65.45	343.25
		2.67	0.65	74.72	327.96
		4.76	0.52	75.66	342.61
		3.14	0.38	78.57	347.96
		2.86	0.21	75.52	316.66
		4.21	0.76	73.57	346.96
		3.55	0.46	66.93	325.43
		2.19	0.69	52.76	316.14
		4.44	0.31	70.54	333.31
		3.03	0.54	65.18	349.46
		2.72	0.24	77.56	298.65
		4.98	0.74	74.61	349.45
		3.37	0.59	70.49	316.91
		2.49	0.36	68.46	311.21
	Group A	12.47	7.62	18.73	101.37
		24.18	4.13	39.16	64.28
		9.86	6.48	27.48	92.56
		17.35	5.09	16.92	73.19
		21.09	7.27	34.57	104.82
		8.72	4.88	22.11	68.41
		19.64	6.95	37.84	88.07
		14.53	5.71	19.05	60.95
		23.77	7.04	28.69	97.63
		10.28	4.36	33.42	79.84

Sample name	Sample source	Dark current before aging/nA	Dark current after aging/nA	X-ray light-dark ratio before aging	X-ray light-dark ratio after aging
$MAPbBr_3$	Our group	23.74	16.42	7.12	22.96
		39.18	9.18	15.18	25.24
		20.67	12.57	8.78	32.17
		34.52	10.06	10.47	15.86
		27.09	15.93	8.64	18.58

		19.83	11.34	4.07	17.34
		38.41	9.79	13.52	32.00
		25.36	14.12	8.43	31.85
		31.95	10.65	15.86	28.43
		22.11	13.08	7.71	34.22
	Group A	42.73	16.73	7.43	26.73
		74.18	27.18	2.68	17.18
		56.09	22.05	6.15	19.06
		63.47	18.47	3.97	17.47
		49.85	25.85	7.88	19.85
		71.22	19.22	4.21	14.22
		40.96	26.64	5.64	16.64
		68.34	17.98	2.93	13.98
		52.61	23.11	6.79	18.11
		73.59	22.59	3.12	15.71
		45.14	16.41	7.06	20.41
		66.88	24.88	4.58	15.88
		58.27	20.27	5.27	22.27
		41.69	22.29	2.74	17.69
		70.03	23.66	6.42	26.03
		54.92	22.92	3.66	18.92
		62.15	18.15	7.91	24.15
		47.36	25.36	4.09	21.36
		69.74	21.74	5.83	19.74
		50.58	19.58	2.61	15.58
	Group B	132.47	37.34	2.74	14.37
		81.23	46.18	7.11	19.18
		118.96	31.07	6.46	12.05
		143.08	43.62	4.09	16.74
		95.51	34.95	7.62	13.91
		109.39	47.41	3.31	10.46
		84.78	39.76	5.08	10.28
		127.12	30.83	4.97	9.83
		140.65	45.09	6.85	10.24
		102.97	36.58	5.24	12.62

Sample name	Sample source	Dark current before aging/nA	Dark current after aging/nA	X-ray light-dark ratio before aging	X-ray light-dark ratio after aging
$Cs_{0.1}FA_{0.9}PbBr_3$	Our group	12.73	3.73	23.57	135.65
		24.18	6.18	33.64	125.23
		18.46	4.05	34.67	107.23
		14.09	3.29	37.08	134.53
		22.62	6.62	18.65	141.62
		13.31	5.11	43.31	137.54
		15.08	4.84	37.77	137.34
		19.97	3.57	36.78	152.18
		20.85	6.39	30.27	136.53

		13.24	5.96	22.49	169.92
		16.56	4.21	43.61	158.71
		24.91	3.88	40.39	175.34
		12.88	6.00	33.15	186.57
		19.12	5.63	25.71	129.45
		21.63	4.77	28.84	141.92
		16.79	3.12	35.26	183.26
		17.14	6.55	23.18	172.43
		23.05	5.28	44.56	123.89
		14.47	4.49	41.93	182.36
		21.68	3.94	29.47	113.74
		12.41	6.71	42.04	143.51
		24.36	5.46	21.88	191.18
		18.07	4.13	24.69	138.09
		15.92	3.69	38.77	160.41
		22.19	6.31	31.02	120.35
		13.77	5.54	40.23	151.83
		16.03	4.24	37.95	177.02
		20.58	3.74	32.59	137.26
		19.45	6.59	27.85	149.68
		14.66	5.36	41.42	153.94
		17.83	4.92	42.88	193.67
		23.91	3.21	36.09	118.52
		12.95	6.08	25.94	154.18
		21.27	5.79	30.94	155.39
		18.64	4.58	22.85	178.85
		15.11	3.47	32.31	160.07
		24.72	6.44	34.46	128.64
		13.58	5.02	23.56	166.85
		20.04	4.66	43.17	170.25
		16.92	3.85	26.72	165.51

Table S3. Benchmarking comparison of representative optimization strategies for perovskite RTSD.

Strategy category	**Representative method**	**ER @662 keV**	**Improvement magnitude**	**Complexity**	**Cost**	**Universality evidence**	**Reference**
Surface	Ammonium bromide passivation	5.7%→1.7%	Medium	Medium	Medium	Single composition	L. Zhao. et al. *Nat. Photon.* **18**, 250-257 (2024).
Surface + architecture	Surface processing + pixelated readout	Overall 1.0%, best single pixel 0.87%		High	High	Theoretically versatile	N. Shen. et al. *Nat. Commun.* **16**, 8113 (2025).
Architecture	Hole-only / unipolar sensing	Best 1.4%		High	High	Specific structure & electronics	Y. He. et al. *Nat. Photon.* **15**, 36-42 (2021).
	Asymmetric metal electrode	Best 3.8%		Medium	Medium	Early baseline milestone	Y. He. et al. *Nat. Commun.* **9**, 1609 (2018).
	Virtual Frisch Grid	Best 1.9%		High	High	Theoretically versatile	H. Qin. et al. *Nat. Commun.* **16**, 158 (2025).
	PIN Junction	Best 1.4%		Medium	Medium	Not reported	X. Wang. et al. *iScience* **26**, 107935 (2023).
Bulk	Purification / zone refining	Best 1.3%		Medium	Medium	Wafer yield stats reported, well versatile	B. Xiao. et al. *Adv. Sci.* **12**, e2501875 (2025).
	Additive-assisted growth	Best 5.5%		High	Medium	Batch / process-specific	Y. Feng. et al. *J. Mater. Chem. C* **8**, 11360-11368 (2020).
	Biasing-induced + bromine in growth	Best 0.7%		Medium	Medium	Material-specific	M. Li. et al. *Nat. Mater.* **24**, 1993-2000 (2025).
	Compositional doping / compensation	12% → 6.5%	Medium	Medium	High	Material-specific	H. Wei. et al. *Nat. Mater.* **16**, 826-833 (2017).
	Growth-defect suppression	Best 2.9%		High	High	65% crystals show “good spectral performance”	L. Zhao. et al. *Nat. Photon.* **17**, 315-323 (2023).
		Best 3.9%		High	High	Composition-specific	Z. Ni. et al. *Adv. Mater.* **36**, e2406193 (2024).
Post-processing	**Bias aging**	**>30% → 2%**	**High**	**Low**	**Low**	**multi-A-site, multi-source**	**This work**

References

[1] P. E. Blöchl, *Phys. Rev. B*, 1994, **50**, 17953–17979.

[2] G. Kresse, J. Furthmüller, *Phys. Rev. B*, 1996, **54**, 11169–11186.

[3] G. Kresse, D. Joubert, *Phys. Rev. B*, 1999, **59**, 1758–1775.

[4] J. P. Perdew, K. Burke, M. Ernzerhof, *Phys. Rev. Lett.*, 1996, **77**, 3865–3868.

[5] J. Klimes, D. R. Bowler, A. Michaelides, *J. Phys.*: *Condens. Mat.*, 2009, **22**, 022201.

[6] M. Gajdoš, K. Hummer, G. Kresse, J. Furthmüller, F. Bechstedt, *Phys. Rev. B*, 2006, **73**, 045112.